Volume 6 · No. 18 – September 20 2010 D15063

NANO MICRO

small

www.small-journal.com

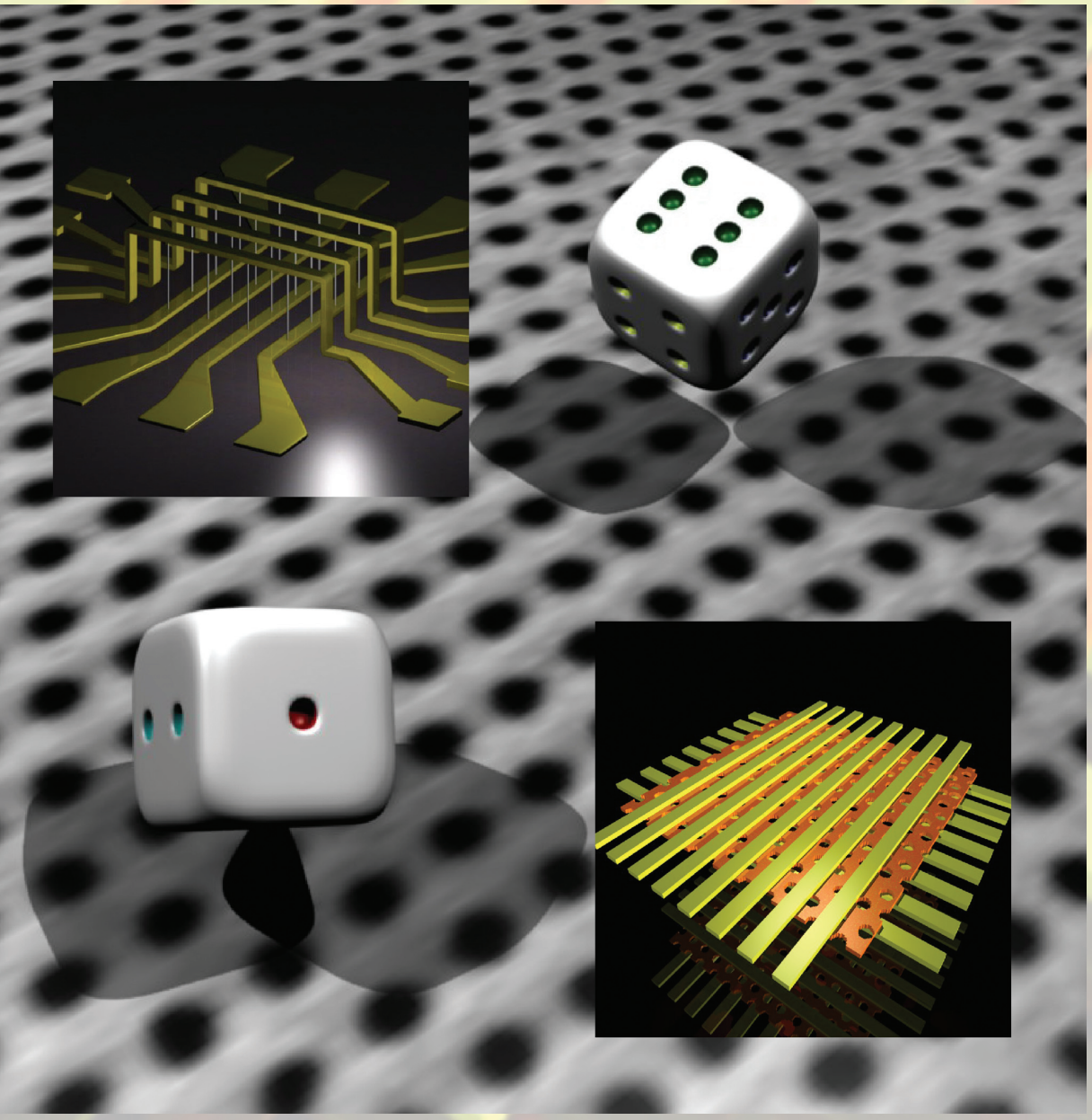

18/2010

WILEY-VCH

Vertical Nanowire Architectures: Statistical Processing of Porous Templates towards Discrete Nanochannel Integration
S. Melinte et al.

small NANO MICRO

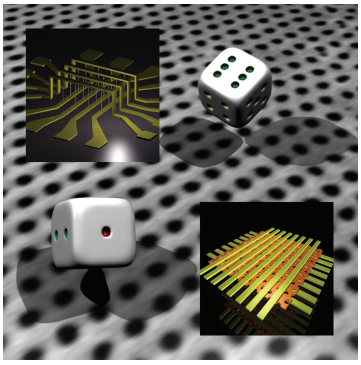

Statistical nanopatterning

How one can devise micro- and nanoporous templates with single-pore resolution? The cover pictures features how a statistical approach provides rigorous selection rules for locating definite sets of objects into random and ordered lattices. The statistical selection method is scalable, and it can be generalized to any type of porous templates for ultimate resolution structuring. Intriguingly, a unified micro- and nanotechnology processing protocol for vertical nanowire crossbar latches in porous alumina templates reduces to a gambling interpretation, following a straightforward, analytical formalism pondered in terms of surface and packing optimization. For more information, please read the Communication "Vertical Nanowire Architectures: Statistical Processing of Porous Templates towards Discrete Nanochannel Integration" by S. Melinte and co-workers, beginning on page 1974.

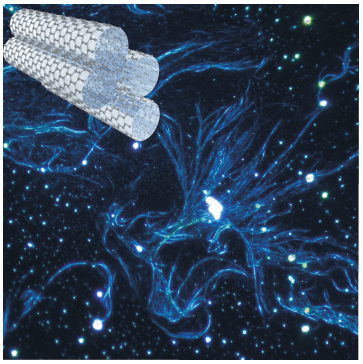

Carbon nanotube characterization

The cover picture shows an optical dark-field microscopy image under normal white light illumination of single-walled carbon nanotubes (SWCNTs) deposited on Si/SiO2 substrates spin-casted from an aqueous detergent solution. The opaque bilayered substrate enables the visualization of the 1D nanoscaled objects, revealing the structure of the SWCNT bundles and providing an easily accessible tool for the localization and retrieval of the SWCNTs. This allows convenient characterization by other spectroscopic and microscopic techniques. Optical bright- and dark- and bright-field visualization techniques are thus greatly facilitating and improving nanotube characterization, as spectroscopic and microscopic information can be directly correlated on the same sample area. For more information, please read the Communication "Optical Visualization of Carbon Nanotubes—A Unifying Linkage between Microscopic and Spectroscopic Characterization Techniques" by A. Hirsch and co-workers, beginning on page 1968.

Nanocrystal assembly

The frontispiece picture shows the formation of a trainlike nanoparticle assembly mediated by tetrakis(4-sulfonatophenyl)porphyrin (TPPS). Linear chains of Au nanorods could be facilely fabricated via the cross-linking of *H*-type TPPS aggregates in solution. The tuning of the plasmon coupling between the Au nanocrystals is demonstrated by varying the porphyrin concentration and thus the interparticle gap distances. The gap distances determined according to the "plasmon ruler equation" agree well with the experimental observations and further confirm the porphyrin-directed assembly process. For more information, please read the Full Paper "Tetrakis(4-sulfonatophenyl)porphyrin-Directed Assembly of Gold Nanocrystals: Tailoring the Plasmon Coupling through Controllable Gap Distances" by C. Z. Huang and co-workers, beginning on page 2000.

coming soon

M. Byun, W. Han, F. Qiu, N. B. Bowden, Z. Lin*
Hierarchically Ordered Structures Enabled by Controlled Evaporative Self-Assembly
DOI: 10.1002/smll.201000816

S. Reisewitz, H. Schroeder, N. Tort, K. A. Edwards, A. J. Baeumner, C. M. Niemeyer*
Capture and Culturing of Living Cells on Microstructured DNA Substrates
DOI: 10.1002/smll.201000776

Look for these important papers in upcoming issues of Small or at www.small-journal.com

All our articles are available online in advance of print. The articles listed here have been judged by either the referees or the editor to be very important, and were immediately copyedited, proofread, and published online. As long as there is no page number available, online manuscripts should be cited in the following manner: Authors, Small, online publication date, DOI number.

small
NANO MICRO

review

Drug delivery

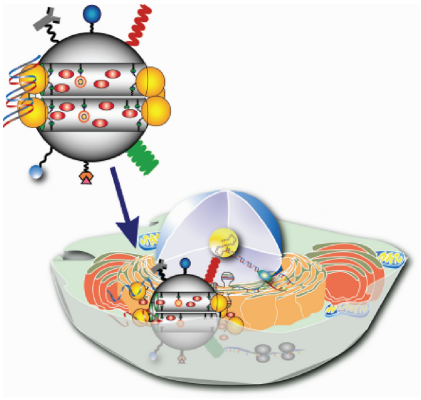

Recent applications of inorganic nanomaterials in the field of drug delivery have attracted a lot of attention in the last decade. One of the most promising candidates for this matter is mesoporous silica nanoparticles. This review highlights the latest progress in terms of the application of mesoporous silica nanoparticles for intracellular drug delivery.

communications

Carbon nanotubes

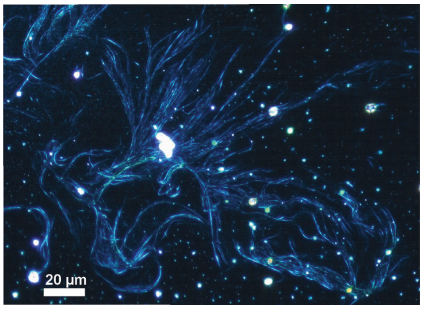

The optical bright- and dark-field visualization (see image) of single-walled carbon nanotubes spin-casted onto Si/SiO_2 substrates with a 300-nm-thick oxide coating is reported. This novel procedure gives access to a low-cost correlation of Raman spectroscopy with microscopic techniques (atomic force microscopy, scanning electron microscopy) greatly facilitating nanotube characterization.

Statistical nanopatterning

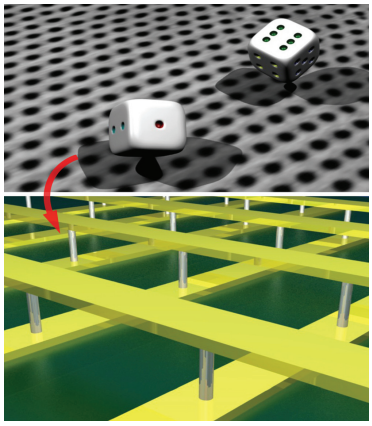

Nanowires and statistics: A statistical process for reading ultradense arrays of nanostructured materials is presented (see image). The experimental realization is achieved through selective nanowire growth using porous alumina templates. The statistical patterning approach is found to provide rigorous selection rules for measuring well-defined numbers of nanowires located into nanoporous templates, and provides a conceptual framework for the fabrication of nanowire-based crossbar latches.

Antireflection behavior

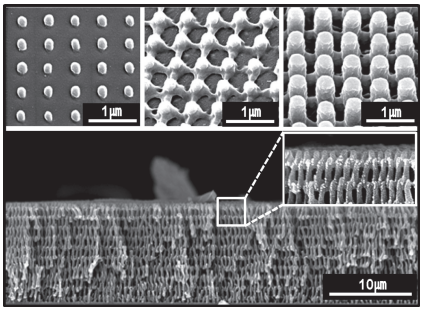

Multidimensional nanostructures that are fabricated by proximity field nanopatterning offer a platform to measure antireflection behavior. Transmittance or opaqueness are gradually changed by controlling the thickness of 3D nanostructures.

Statistical nanopatterning

Vertical Nanowire Architectures: Statistical Processing of Porous Templates Towards Discrete Nanochannel Integration

Alexandru Vlad, Sorin Melinte, Mária Mátéfi-Tempfli, Luc Piraux, and Stefan Mátéfi-Tempfli*

While the process simplicity, the variety of synthesized systems, and the order control over large areas have led nanoporous materials[1–9] to the top of nanotechnology fabrication strategies, the major drawback that restricts their integration into devices is the mismatch between their characteristic sizes and present technological ability. General characterization approaches have studied large assemblies of nanostructures fabricated inside templates or single nano-objects.[10–16] Though they provided breakthrough results, these techniques essentially exploit the reduced dimensionality rather than the high density imposed by the nanoporous templates. In templateless synthesized systems, such as epitaxially grown semiconductor nanowires,[17–20] carbon nanotubes,[21,22] or various chemically designed functional nanostructures,[23,24] the dense vertical packing and order are often neglected as the subsequent device integration proceeds through the destruction of the initial fabricated morphology followed by planar repositioning of only few nanostructures. The number of integrated nanowires – as compared to the quantity of the synthesized ones – is thus small. It may be more interesting to grow nanowires in ultradense vertical architectures and read well defined numbers of nanowires.

Interestingly, nanotechnology's armamentarium includes few methods that are random by nature, in which an *item* (e.g., a scanning-probe tip or a nanoengineered opening) is arbitrarily positioned relative to a porous template with the prospect of interrogating a single grown nanowire.[11,25–27] In fact, these random approaches can be extended to other ordered or disordered nanostructured lattices, scaled, and readily made parallel. For example, the current-sensing atomic force microscopy (AFM) technique developed by Russell and coworkers[11] to characterize vertical conductive polymer nanowires can be adapted to more than one scanning-probe tip using the "Millipede" concept proposed by IBM. This technology operates thousands of AFM tips in parallel with terabit data-storage capacity and, besides accessing single nanopores, could be elegantly applied to the patterning of nanoporous templates following the same rationale.[28] The optimization of statistical methods for ultralarge-scale vertical integration is difficult. For example, the hexagonal lattice – a prototypical self-ordering geometry – is considered to be severely incompatible with the square arrangements requested by industry-standard circuits.[29] While valuable methods to guide the self-assembly behavior towards complex patterns at the nanoscale are continuously improving,[30–32] several technological aspects remain to be addressed in order to satisfy the state-of-the-art of dimensional and positional control needed by semiconductor manufacturing.

In this Communication, we address a general route for the integration of single vertical nanowires in architectures denominated as vertical nanowire crossbar latches (VNCLs). We demonstrate the integration of single vertical metallic nanowires[33] and we propose a methodology to statistically devise porous templates with single-nanopore resolution, useful for integrating a large amount of nanowires via parallel processing. For exemplification, we employ supported porous anodic alumina oxide (AAO) membranes as nanostructuring templates.[10] The synthesized nanowires remain embedded in the host matrix and we achieve accurate control over the number of grown and electrically connected nanowires. Obviously, the selection of nanopores in a nanoporous template could be achieved by performing a preliminary overlay-alignment analysis but it would require laborious work and time-consuming protocols. By using statistical processing, these inconveniences are avoided. We address by experiments, within a simple theoretical framework, several fundamental aspects of the statistical processing of nanoporous templates. Building on statistical patterning, we further develop a complete processing protocol for VNCL fabrication based on alumina templates.

Statistical patterning: We consider first the single-nanopore resolution that can be achieved by selective mask structuring of AAO templates.[26,27] The patterning here is purely random due to the absence of mask-overlay alignment, as shown in the scanning electron microscopy (SEM) images

Dr. A. Vlad, Dr. S. Melinte
Institute of Information & Communication Technologies
Electronics and Applied Mathematics (ICTEAM)
Université Catholique de Louvain (UCL)
Place du Levant 3, Louvain-la-Neuve, B-1348, Belgium
E-mail: sorin.melinte@uclouvain.be
M. Mátéfi-Tempfli, Prof. L. Piraux, Dr. S. Mátéfi-Tempfli
Institute of Condensed Matter and Nanosciences (ICMN)
Université Catholique de Louvain (UCL)
Place Croix du Sud 1, Louvain-la-Neuve, B-1348, Belgium

DOI: 10.1002/smll.201000723

NANO MICRO small

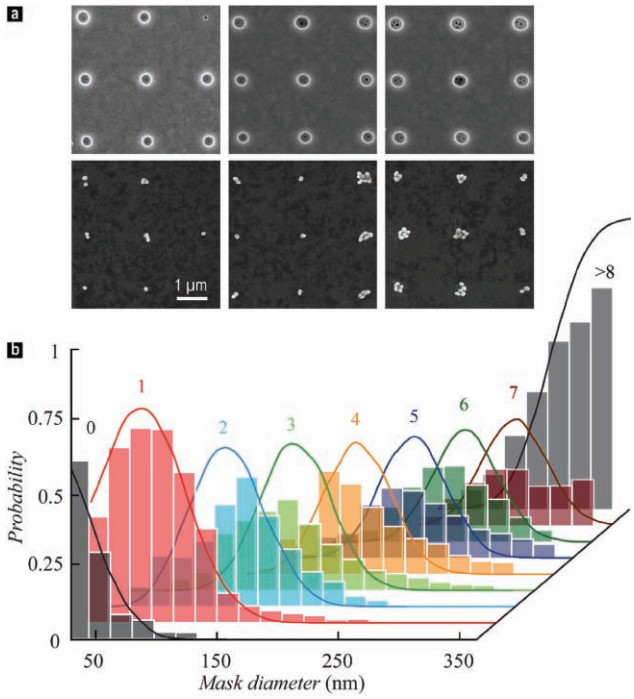

Figure 1. Experiments on statistical patterning. a) Top-view SEM images of patterned masks with gradually increased sizes (top) and the statistically achieved resolution (bottom). b) Experimental histograms and simulated probability distributions for selection and processing of a given number of nanopores inside an alumina template with short-range pore ordering. For the sake of clarity, the histograms and the calculated curves are shifted. The mask-size cutoff is 30 nm. The mean pore diameter and interpore distance are ≈72 and 132 nm, respectively.

in **Figure 1**a. Intuitively, one can reason that the number of revealed nanopores in the lithographic process will depend on the geometry and size of the mask. Indeed, as displayed in Figure 1b, a definite resolution probability could be achieved for a given range of circular-mask diameters. Note that the patterning resolution (from 0 to >8) is given in our experiments as the number of the subsequent nanowires grown into revealed nanopores. Conceptual understanding of this manufacturing path simply reduces to counting the number of nanopores inside a region of interest, arbitrarily selected from an image that describes the morphology of the template. The good agreement between the experiment and the simulation of the patterning process proves that, fundamentally, there is no preference to any of the specific sites on templates. Remarkably, the single-nanopore resolution is realized with a yield as high as 70% at a mask diameter of ≈70 nm for the considered case (red histogram in Figure 1b). Furthermore, it interferes only with null- (≈9%), double- (≈18%), and triple-pore (<3%) patterning resolutions.

Downscaling the template features will primarily translate into a left-side shift of the probability peak position accompanied by a reduction of the full-width at half maximum (**Figure 2**a,b). In turn, nanopore ordering has an intriguing influence on the selection probabilities (Figure 2c,d). A preferential behavior for some nanopore-resolution numbers (3, 4, and 7) together with a detrimental effect on the others (2, 5, and 6) can be observed. This correlates to the radial symmetry of the circular mask and the hexagonal packing of the nanopores. Compared to the short-range-ordered template, the single-pore patterning resolution at its maximum expectation overlaps, to a lesser extent, only with null- and double-pore resolutions and attains a higher yield of 90%. Notably, a rectangular mask—defined by the intersection of two orthogonally crisscrossed stripes—does not significantly alter the probability distribution (Figure 2e,f). The single-nanopore-resolution maxima for a highly ordered alumina template using a circular and a square mask are attained at 66-nm diameter and 50-nm lateral size, respectively. Reckoning on 50-nm-wide stripes, recently addressed by the crossbar-latch technology proposed by Hewlett Packard,[33] the single-nanopore resolution probability reaches 90%. As such, a clear enhancement of the 1-, 3-, 4-, and 7-pore patterning resolutions can be observed upon ordering of the nanopores as well as the minimal influence upon the single-nanopore resolution exerted by modification of the mask geometry.

Analytical interpretation of statistical patterning. For the mathematical representation of the patterning process, a perfect triangular lattice was generated (Figure 2g–i) and its probability distributions were simulated (Figure 2j, open circles). Here, d is the pore diameter and h is the interpore distance. The dashed circles delimit the pores (d = 60 a.u. and h = 120 a.u.) and the gray circle represents a circular mask with diameter D. The intersection occurrence of the mask with a pore of the triangular lattice is proportional to the area generated by a *virtual* circle of diameter $D + d$, concentric with the pore. The intersection area of 2, 3, and so on, circles is subsequently proportional to the probability of double-, triple-, and so on, nanopore resolutions. A given probability is thus a fraction of the surface area for a definite type of intersection. Due to the triangular symmetry, the calculations can be simplified and limited to the elementary cell (solid triangle in Figure 2g–i). For case I (Figure 2g), only null- and single-pore resolutions are expected and the analytical functions describing the probabilities are

$$P_0^I = 1 - P_1^I \tag{1}$$

and

$$P_1^I = \frac{\pi\sqrt{3}}{6}\left(\frac{D+d}{h}\right)^2 \tag{2}$$

Obviously, the square-power-law distribution described by Equation 2 has no local maxima and hence neither does the single-pore resolution. Actually, the first maximum occurs for case II (Figure 2h), when the overlap of two virtual circles marks the onset for the double-pore patterning resolution. The probability functions can be written as

$$P_0^{II} = 1 - P_1^{II} - P_2^{II}, \tag{3}$$

$$P_1^{II} = \frac{\pi\sqrt{3}}{6}\left(\frac{D+d}{h}\right)^2 - 2P_2^{II}, \tag{4}$$

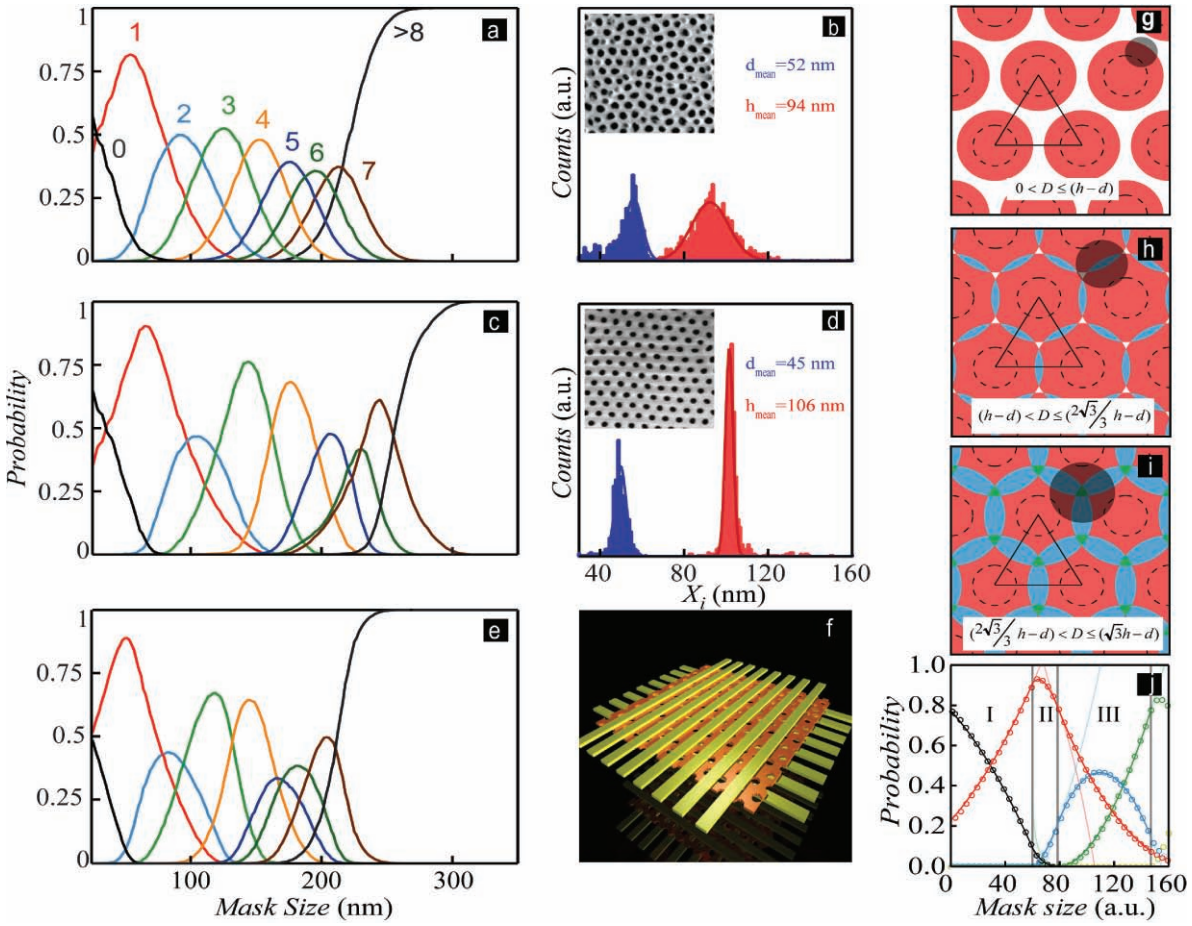

Figure 2. Analytical interpretation of statistical patterning. a) Simulated probability distributions for an AAO template with short-range pore ordering and a lower interpore distance than presented in Figure 1b. b,d) Histograms of the pore-diameter (*d*, blue) and interpore-distance (*h*, red) distributions for the templates used. Insets show 1 μm × 1 μm SEM images depicting the surface morphology. Probability distribution for a highly ordered AAO template using c) a circular and e) a square mask, respectively. f) Schematized view of the square mask envisioned as the intersection of perpendicular stripes in a crossbar latch patterned on different sides of the template. g–i) Surface-plot representations of the statistical-structuring methodology. The dashed circles delimit the pores ($d = 60$ a.u., $h = 120$ a.u.) and the gray circle represents the circular mask of diameter *D*. The colors white, red, blue, and green correspond to the probabilities for null-, single-, double-, and triple-pore resolutions, respectively. j) Simulated (dots) and analytically computed (curves) probability distributions. The color code has a double significance: it represents the surface-area fraction for each finite pore resolution and it delimits the loci of the mask center needed to achieve it. The vertical gray lines are the boundary conditions for cases I, II, and III corresponding to surface -plot representations of the statistical structuring in (g–i), respectively.

and

$$P_2^{II} = \sqrt{3}h^{-2}\left\{(D+d)^2\cos^{-1}\left(\frac{h}{D+d}\right) - h\sqrt{(D+d)^2 - h^2}\right\}, \quad (5)$$

where P_0^{II}, P_1^{II} and P_2^{II} represent, respectively, null-, single- and double-pore resolutions. Indeed, P_1^{II} reaches a maximum and then monotonically decreases. Continuing further to case III (Figure 2i), marked by the overlap between three virtual circles, we observe the onset for P_3^{III}, while P_0^{III} completely vanishes. Concomitantly, P_1^{III} continues to decrease whereas P_2^{III} passes through a maximum. We skip more elaborate analytical equations but, following the same principle, the calculation can be extended to any diameter *D* of interest. For realistic statistical nanostructuring, the pores and the mask cannot be described by perfect circles and the regular arrangement is disturbed. However, the analytical approach remains the same for less-ordered templates or even random lattices. There will be always a finite probability for null- and double-nanopore patterning resolutions at the maximum expectation of the single-pore resolution and this holds true for any pore-size distribution. Hexagonal packing of the pores in a template seems to provide the highest probability of achieving the single-nanopore resolution using the statistical approach.[34] Indeed, the surface-plot representation is similar to Thue's theorem: no packing of nonoverlapping discs of equal size in a plane has a higher density than that of the hexagonal packing. For example, a perfect square lattice will have a maximum probability of compared to for the hexagonal lattice (provided that both of them are bearing circular pores). The probability of 0.904 obtained for single-pore resolution, as calculated on the fabricated ordered templates (Figure 2c), is very close to the ideal value. This corroborates the high ordering degree of the template and highlights the robustness of the statistical procedure against the structural inhomogeneities of the template via smearing and averaging effects.

small NANO MICRO

Reading well defined numbers of nanowires by statistical patterning. Based on this analysis, we were able to select and integrate a precise number of metallic nanowires in alumina-based VNCLs. A schematic of the fabrication process is shown in **Figure 3**a and the fabrication details are provided in the Experimental Section. Basically, our method reduces to the fabrication of a microchip-supported AAO nanoporous membrane and subsequent micro- and nanoprocessing of the AAO slab for the growth and electrical connection of a statistical assembly of nanowires. An optical image of a processed microchip-supported AAO membrane is shown in Figure 3d. The circuitry design is simple: an array of metallic stripes with external bonding pads working as bottom electrodes (BEs) and, orthogonally to them, an array of incomplete metallic tracks for the top electrodes (TEs) definition. At the beginning of the VNCL-fabrication process, the anodization results in a circular AAO nanoporous membrane surrounded by the initial conducting Al film. For the statistical structuring, the surface morphology of the nanoporous template plays a crucial role. A postanodization enlargement step is compulsory as it drastically changes the surface morphology of the alumina film (Figure 3b,c). Consequently, the statistical distribution of the number of accessed nanowires will be established. To avoid electrical shorting on the BEs, the anodization of the Al layer has to be complete, implying resistances of the order of MΩ between different BEs. Electroplating at this stage will occur in a self-aligned way all over the electrically conductive areas in contact with the aluminum.

In this configuration, all of the electrodes (BEs and TEs) are, in principle, electrically shunted through the surrounding Al layer and a structuring step is required to decouple them. The process is based on the wet-etch chemistry of the AAO and aluminum layer. Aqueous potassium hydroxide solution was used to etch both components using a silicon nitride mask. The etching was found to occur in a highly anisotropic way (Figure 3e,f). The specificity of the present process dictated a particular microchip layout, as presented in Figure 3g. The electrochemical growth requires an electrical connection between the macroscopic electrode and the plating area. This is realized by using the remaining Al layer after the anodization. A macroscopic contact pad (Al) was defined on the edge of the chip to facilitate the interface with the electrochemical setup (noted as the "electroplating contact" in Figure 3g). A stripe was also defined connecting the latter to the BEs. Their number and position (black arrows) can be controlled using splitters (white arrow) defined during the patterning step. At this point, the device integration of single nanowires could be performed using statistical structuring.

Besides the available useful protocol for the precise growth and selection of nanowires, a reliable procedure for the realization of the electrical contacts is needed. Here, for contacting nanowires, we adopted a well known strategy

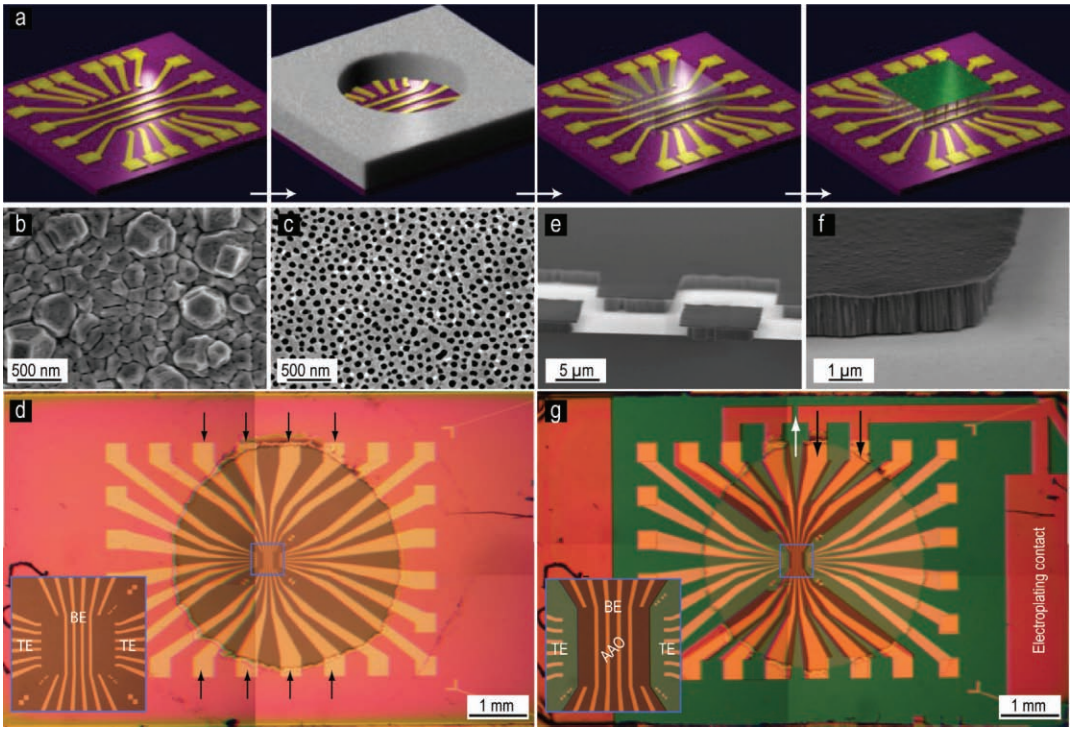

Figure 3. Micro- and nanostructuring of alumina membranes. a) Schematic view of the process flow for the fabrication of VNCLs based on alumina membranes. SEM views of the alumina surface b) before and c) after the enlargement step. d) Optical microscopy view of the processed chip after the anodization step. The anodization area is dimensioned such that it overlaps the BEs. Inset: magnified close up of the central area. The precursor wirings for the TEs are visible. e,f) Side-view SEM images of the etched alumina slabs bearing the silicon nitride mask on top. The anisotropic etching profile is visible. g) Macroscopic view of the chip after the alumina/aluminum slab patterning. The working BEs are entirely protected by alumina and electrically connected to the electroplating pad through the aluminum slab. Some of the BEs can be disconnected from the electroplating contact during this step (white arrow). Inset: close up on the central area. The TEs and alumina-covered BEs are visible.

based on the use of a self-contacting layer (SCL).[35] The SCL, consisting of a thin Au film, was grown specifically in the areas where the selective electroplating was to be performed. It is key to confine the SCL on the AAO membrane; examples of the masks used and SCLs obtained are shown in **Figure 4**a–d.

Subsequently, six selective electroplating masks with nominal diameters of ≈300 nm were patterned onto the SCL above the working BEs. After the predeposition enlargement step, an extremely reduced number of Ni nanowires were plated on each sample (≈50, as expected by the processing statistics and assuming that no parasitic growth sites are present). Once the nanowires were contacting the SCLs, small jumps in the plating current could be observed (not shown here). Typically, all of the six SCLs were connected and a Ni "mushroom cap" was formed on each plated area. Subsequently, the masking layer protecting the SCL was stripped to expose the underlying gold film, which was electrically connected to the nanowires. Due to the sharply bent profile of the patterned AAO film (Figure 3e,f), metal deposition at a tilt angle was again required for the fabrication of TEs. The fabrication protocol was identical to that for the SCL patterning with the exception of the design (lines connecting the opposite precursor metallic pads of TEs and covering the SCL). A ±45° tilt angle was used to deposit 1 μm of Al. An example of a conformal coated AAO step edge is shown in Figure 4e. A thick metal coating was used because of the relatively nonuniform profile of the AAO slab sidewalls. This step finishes the processing of crossbar devices with single nanowires connected at each crosspoint (Figure 4f).

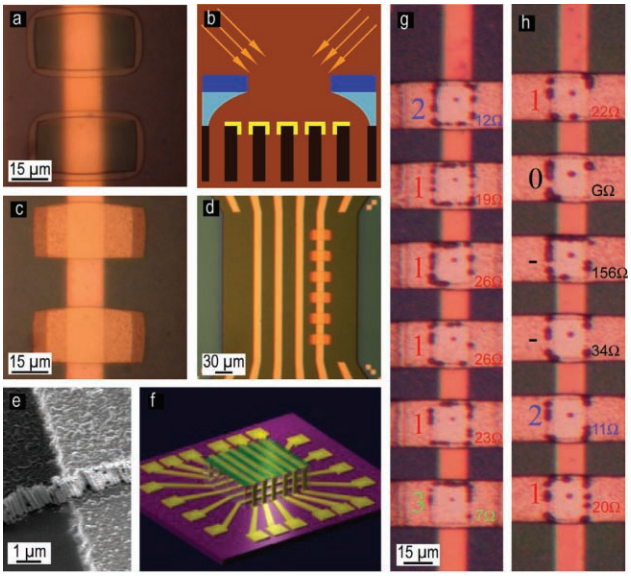

Figure 4. VNCL fabrication. a) Top-view optical micrograph of the overexposed resist for the top-electrode definition. b) Schematic view of the tilt-angle evaporation technique employed. c,d) Close-up and large views of the central part of the chip after the SCL definition. e) Tilted SEM view of a top electrode surmounting the AAO edge. The shadowed area during tilt-angle metal deposition is visible. f) Schematic view of the final device. g,h) Optical micrographs of two fabricated 1 × 6 crossbar devices. The central black spots are the caps of flooded Ni nanowires. A 50% yield to connect a single nanowire was achieved.

Though we can statistically estimate the number of grown nanowires by knowing the morphology of the template and the size and shape of the mask, the number of electrically contacted nanowires was precisely determined by measuring the resistance of each crossbar point. The expected resistance for a single Ni nanowire (assuming a bulk resistivity of 7×10^{-8} Ω m, a diameter of 80 nm, and a height of 1.5 μm) is 21 Ω. On half of the crosspoints, approximately the same resistance was measured (as noted in Figure 4g,h). The small variations could be attributed to differences in contact resistance as well as variations in the nanowire diameter. Deficient crosspoints have been also detected as well as doubly or triply connected nanowire sites. Intriguingly, this suggests that the SCL has a "cheating" effect on the nanowire-growth "gambling": it reduces the contacting statistics to one nanowire. While it is possible to statistically control the number of grown nanowires, contacting a single nanowire is ensured by the presence of the SCL.

In summary, we have resolved single features within nanoporous templates by statistical processing. By adjusting only the size of the lithographic mask, precise control over the patterning resolution can be achieved without any complex preliminary analysis or overlay alignment. The described approach was developed in order to integrate single nanowires, fabricated using electrochemical methods, into the nanopores of AAO membranes for the development of high-density crossbar latches. The statistical approach may have potential for other material-deposition methods (electroless plating and chemical or physicochemical growth)[36,37] or even flexible templates.[38] The statistical patterning could be an interesting alternative to micro- or nanoprocessing approaches that reduce to sectoring the surface of a nanoporous material with a masking item.

Experimental Section

Statistical experiment protocol: Detailed experimental description can be found elsewhere.[26,27] Briefly, porous AAO templates were fabricated by anodizing aluminum in 0.3 M oxalic acid at 40 and 60 V while keeping the substrate at 2 °C. Short-range-ordered AAO was fabricated in a single-step anodization, while ordered AAO was fabricated in a double-step processing. Qualitative analysis of the AAO templates (mean pore diameter, interpore distance, and ordering degrees) was based on a Delaunay tessellation and has been detailed elsewhere.[39] Selective-site electroplating was realized by patterning a 350-nm-thick silicon nitride mask deposited on top of AAO. Circular masks with diameters (D_{exp}) ranging from 30 to 500 nm, defined using electron beam lithography (EBL) and reactive ion etching (RIE), were used for the statistical study of the selective AAO patterning. The electrodeposition of the Ni nanowires within the exposed areas was carried out using an EG&G PAR 263 Potentiostat (Princeton Applied Research) in a conventional three-electrode cell with a Pt counter electrode and Ag/AgCl as the reference electrode. In order to ensure homogeneous growth, the pulse-plating method was used to deposit the Ni nanowires from a solution containing $NiSO_4$ (0.5 M) and H_3BO_3 (0.5 M) at room temperature (repetitive pulses: –1.05 V for 10 ms [deposition] and –0.70 V for 90 ms [standby]). Partial template filling was realized

small NANO MICRO

in order to obtain nanowires of ≈600 nm in height. After the electroplating and AAO removal, the samples were inspected by SEM. SEM images were taken with a resolution of 640 × 520 pixels and the image analysis was performed with a resolution better than 5 nm. The number of events corresponding to the observation of a fixed number of nanowires for a mask diameter D_{exp} was counted with the D_{exp} bin being set to 18 nm. The data accumulated for each bin was divided by the total number of events within the respective bin to obtain the probability. About 1100 events were included in the histogram shown in Figure 1b.

Statistical-computation protocol: The probability of having *N* nanopores inside a circular mask at various locations on the AAO surface was computed using image-analysis routines provided by Igor Pro software (Wave Metrics Inc.). A circular or square region of interest (ROI) was generated on top of binarized SEM images and the number of nanopores inside the ROI was counted. For the computation, a counting threshold was introduced. If the intersection of the ROI with a pore displayed by the SEM image is less than the threshold value (defined as counting threshold × mean pore area), the pore is accounted as 0; otherwise it is accounted as 1. For the statistical patterning of the AAO templates, the counting threshold was fixed to 0.02 (Figure 1b).

VNCL-fabrication protocol: Thermally oxidized silicon wafers, with a grown 300-nm-thick SiO_2 layer, were used as fabrication platforms. Physical metal-vapor deposition followed by photolithography and wet chemical etching of the metal layer were employed to pattern the metallic tracks. Typically, they were made in Au (50-nm thick) with a Ti adhesion layer (5-nm thick). Next, Al was deposited covering the entire surface of the sample. An intermediate 5-nm Ti adhesion layer was used. Single-step anodic oxidation of the 1–2-μm-thick Al layer was performed in $H_2C_2O_4$ (0.3 M) at 60 V using a two-electrode cell at 2 °C. A two-step enlargement was found to provide good reproducibility in the processing, consistent with the statistical interpretation: 80–90% of the nominal values shortly after the anodization and the rest prior to the electroplating. The pores were enlarged in an orthophosphoric acid solution (0.5 M) at 30 °C (typically 40 min for a pore diameter of ≈70 nm). The postanodization enlargement step is compulsory as it drastically changes the surface morphology of the alumina film (see Figure 3b,c) and hence the statistical distribution of the number of accessed nanowires will be affected. The enlargement step prior to the electroplating does not crucially alter the alumina-surface morphology; basically, only the diameters of the pores are slightly increased. After the anodization, the samples were cleaned in acetone with 1 –2 min of ultrasonication to remove any surface residuals. Next, a 400-nm-thick plasma-enhanced chemical vapor deposition (PECVD) SiN_x film was deposited and a 1-μm-thick poly(methyl methacrylate) (PMMA) film was used to pattern and transfer the desired design onto the SiN_x layer using EBL and RIE. The SiN_x deposition was carried out at a pressure of 0.8 mTorr and a radio-frequency power density of 60 mW cm^{-2}. The gas composition was $SiH_4/NH_3/N_2$ with corresponding mass flows of 500/2/750 sccm. The thickness of the SiN_x layer was determined by surface profilometry and ellipsometry. In order to avoid metal interdiffusion in the underlying conductive layers, the deposition step was performed by keeping the substrate temperature below 150 °C. Following silicon nitride patterning, the samples were immersed in KOH solution and left until complete removal of the Al layer. The remaining Ti and TiO_x layers were removed using a 2% HF solution. The remaining SiN_x was subsequently stripped using RIE (CHF_3/SF_6 with corresponding mass flows of 50/0.5 sccm, 30 mTorr pressure, and 0.15 W cm^{-2} radio-frequency power density). For the fabrication of the SCL, an overexposed, double-layer resist stack was used consisting of 2-μm PMMA(8.5)MAA copolymer (a mixture of PMMA and 8.5% methacrylic acid) and 1-μm PMMA, 1000 μC cm^{-2}. The large undercut can be visualized in Figure 4a and it extends in the PMMA(8.5)MAA layer for 3–5 μm with respect to the top PMMA layer. For a 3-μm resist stack, a 3-μm undercut allows the metal to evaporate at 45° tilt. The sample tilting was performed in situ: 2+2 nm of Ti followed by 20 + 20 nm of Au were evaporated successively at ±45° with respect to the sample normal. The sample was placed such that the beam-arrival direction was perpendicular to the axis of the BEs From geometrical considerations, the maximum penetration depth of the metal along the pores equals the diameter of the pores (here, ≈80 nm). After lift-off removal of the remaining resist, the samples were processed for the selective growth of nanowires only on top of the SCL. PECVD was used to protect the AAO surface with a 300-nm-thick SiN_x film. EBL was subsequently used to define 100-nm holes in a 200-nm-thick PMMA layer and then the pattern was transferred to the SiN_x layer using RIE. The predeposition enlargement step was performed by short soaking the samples in 0.5 M H_3PO_4 at 30 °C for 5 min. The electrodeposition of Ni nanowires within the exposed areas was carried out according to the above-explained statistical experiment protocol.

Acknowledgements

This work was supported by the NANOMOL and TINTIN projects (Communauté Française de Belgique), the NANOTIC programme (Région Wallonne), Science Policy Office of the Belgian Federal Government (PAI 6/42), the SUNTUBE project (Région Wallonne), and the Belgian National Fund for Scientific Research (FRS-FNRS) via F.4501.05 grant and FRFC projects 2.4.505.09 and 2.4.546.08F.

[1] C. R. Martin, *Science* **1994**, *266*, 1961.
[2] C.-G. Wu, T. Bein, *Science* **1994**, *264*, 1757.
[3] P. Mansky, P. Chaikin, E. L. Thomas, *J. Mater. Sci.* **1995**, *30*, 1987.
[4] S. B. Darling, *Prog. Polym. Sci.* **2007**, *32*, 1152.
[5] W. Lee, R. Ji, U. Gösele, K. Nielsch, *Nat. Mater.* **2006**, *5*, 741.
[6] T. Thurn-Albrecht, J. Schotter, G. A. Kästla, N. Emley, T. Shibauchi, L. Krusin-Elbaum, K. Guarini, C. T. Black, M. T. Tuominen, T. P. Russell, *Science* **2000**, *290*, 2126.
[7] C.-A. Fustin, P. Guillet, U. S. Schubert, J.-F. Gohy, *Adv. Mater.* **2007**, *19*, 1665.
[8] G. Meng, Y. I. Jung, A. Cao, R. Vajtai, P. M. Ajayan, *Proc. Natl. Acad. Sci. USA* **2005**, *102*, 7074.
[9] M. Li, R. B. Bhiladvala, T. J. Morrow, J. A. Sioss, K.-K. Lew, J. M. Redwing, C. D. Keating, T. S. Mayer, *Nat. Nanotechnol.* **2008**, *3*, 88.
[10] a) M. Tian, S. Xu, J. Wang, N. Kumar, E. Wertz, Q. Li, P. M. Campbell, M. H. W. Chan, T. E. Mallouk, *Nano Lett.* **2005**, *5*, 697; b) O. Rabin, P. R. Herz, Y.-M. Lin, A. I. Akinwande, S. B. Cronin, M. S. Dresselhaus,*Adv. Funct. Mat.* **2003**, *13*, 631; c) Z. Zhang, X. Sun, M. S. Dresselhaus, J. Y. Ying, J. Heremans, *Phys. Rev. B* **2000**, *61*, 4850.

[11] J. I. Lee, S. H. Cho, S.-M. Park, Jin K. Kim, Jai K. Kim, J.-W. Yu, Y. C. Kim, T. P. Russell, *Nano Lett.* **2008**, *8*, 2315.
[12] P. Banerjee, I. Perez, L. Henn-Lecordier, S. B. Lee, G. W. Rubloff, *Nat. Nanotechnol.* **2009**, *4*, 292.
[13] A. J. Hong, C.-C. Liu, Y. Wang, J. Kim, F. Xiu, S. Ji, J. Zou, P. F. Nealey, K. L. Wang, *Nano Lett.* **2010**, *10*, 224.
[14] L. Gence, S. Faniel, C. Gustin, S. Melinte, V. Bayot, V. Callegari, O. Reynes, S. Demoustier-Champagne, *Phys. Rev. B* **2007**, *76*, 115415.
[15] L. Qin, S. Park, L. Huang, C. A. Mirkin, *Science* **2005**, *309*, 113.
[16] P. A. Smith, C. D. Nordquist, T. N. Jackson, T. S. Mayer, B. R. Martin, J. Mbindyo, T. E. Mallouk, *Appl. Phys. Lett.* **2000**, *77*, 1399.
[17] A. Javey, S. W. Nam, R. S. Friedman, H. Yan, C. M. Lieber, *Nano Lett.* **2007**, *7*, 773.
[18] D. Whang, S. Jin, Y. Wu, C. M. Lieber, *Nano Lett.* **2003**, *3*, 1255.
[19] K. A. Dick, K. Deppert, M. W. Larsson, T. Martensson, W. Seifert, L. R. Wallenberg, L. Samuelson, *Nat. Mater.* **2004**, *3*, 380.
[20] X. Duan, Y. Huang, Y. Cui, J. Wang, C. M. Lieber, *Nature* **2001**, *409*, 66.
[21] Y. Hayamizu, T. Yamada, K. Mizuno, R. C. Davis, D. N. Futaba, M. Yumura, K. Hata, *Nat. Nanotechnol.* **2008**, *3*, 289.
[22] S. Talapatra, S. Kar, S. K. Pal, R. Vajtai, L. Ci, P. Victor, M. M. Shaijumon, S. Kaur, O. Nalamasu, P. M. Ajayan, *Nat. Nanotechnol.* **2006**, *1*, 112.
[23] L. Manna, D. J. Milliron, A. Meisel, E. C. Scher, A. P. Alivisatos, *Nat. Mater.* **2003**, *2*, 382.
[24] P.-E. Trudeau, M. Sheldon, V. Altoe, A. P. Alivisatos, *Nano Lett.* **2008**, *8*, 1936.
[25] L. Piraux, K. Renard, R. Guillemet, S. Mátéfi-Tempfli, M. Mátéfi-Tempfli, V. A. Antohe, S. Fusil, K. Bouzehouane, V. Cross, *Nano Lett.* **2007**, *7*, 2563.
[26] A. Vlad, M. Mátéfi-Tempfli, S. Faniel, V. Bayot, S. Melinte, L. Piraux, S. Mátéfi-Tempfli, *Nanotechnology* **2006**, *17*, 4873.
[27] A. Vlad, M. Mátéfi-Tempfli, V. A. Antohe, S. Faniel, N. Reckinger, B. Olbrechts, A. Crahay, V. Bayot, L. Piraux, S. Melinte, S. Mátéfi-Tempfli, *Small* **2008**, *4*, 557.
[28] P. Vettiger, M. Despont, U. Drechsler, U. Dürig, W. Häberle, M. I. Lutwyche, H. E. Rothuizen, R. Stutz, R. Widmer, G. K. Binning, *IBM J. Res. Develop.* **2000**, *44*, 323.
[29] International Technology Roadmap for Semiconductors, http://www.itrs.net/Links/2007ITRS/Home2007.html.
[30] H. Masuda, H. Asoh, M. Watanabe, K. Nishio, M. Nakao, T. Tamamura, *Adv. Mater.* **2001**, *13*, 189.
[31] J. Y. Cheng, A. M. Mayes, C. A. Ross, *Nat. Mater.* **2004**, *3*, 823.
[32] C. Tang, E. M. Lennon, G. H. Fredrickson, E. J. Kramer, C. J. Hawker, *Science* **2008**, *322*, 429.
[33] P. J. Kuekes, D. R. Stewart, R. S. Williams, *J. Appl. Phys.* **2005**, *97*, 034301.
[34] D. Mackenzie, *Science* **1999**, *285*, 1338.
[35] S. Michotte, S. Mátéfi-Tempfli, L. Piraux, *Appl. Phys. Lett.* **2003**, *82*, 4119.
[36] A. Vlad, C. A. Dutu, P. Guillet, P. Jedrasik, C.-A. Fustin, U. Södervall, J.-F. Gohy, S. Melinte, *Nano Lett.* **2009**, *9*, 2838.
[37] A. Vlad, S. Yunus, A. Attout, Dana A. Serban, L. Gence, S. Faniel, J.-F. Gohy, P. Bertrand, S. Melinte, *Small* **2010**, *6*, 627.
[38] S. Mátéfi-Tempfli, M. Mátéfi-Tempfli, *Adv. Mater.* **2009**, *21*, 4005.
[39] S. Mátéfi-Tempfli, M. Mátéfi-Tempfli, L. Piraux, *Thin Solid Films* **2008**, *516*, 3735.

Received: April 28, 2010
Revised: June 19, 2010
Published online: August 18, 2010

